sustainability

MDPI

Article

Performance Improvement of a Novel Trapezoid Air-Cooling Battery Thermal Management System for Electric Vehicles

Gang Zhao [1], Xiaolin Wang [1,*], Michael Negnevitsky [1], Hengyun Zhang [2] and Chengjiang Li [3,4]

[1] School of Engineering, University of Tasmania, Hobart, TAS 7005, Australia; gang.zhao@utas.edu.au (G.Z.); michael.negnevitsky@utas.edu.au (M.N.)
[2] School of Mechanical and Automotive Engineering, Shanghai University of Engineering Science, 333 Longteng Road, Songjiang, Shanghai 201620, China; zhanghengyun@sues.edu.cn
[3] School of Management, Guizhou University, Guiyang 550025, China; chengjiang.li@utas.edu.au
[4] Key Laboratory of "Internet+" Collaborative Intelligent Manufacturing in Guizhou Province, Guiyang 550025, China
* Correspondence: xiaolin.wang@utas.edu.au

Abstract: An air-cooling battery thermal management system is a reliable and cost-effective system to control the operating temperatures of the electric vehicle battery pack within an ideal range. Different from most designs of the rectangular battery pack in previous research, this one proposed a novel isosceles trapezoid layout to improve system heat dissipations. The simulation results showed that the trapezoid design delivered better cooling performances than the rectangular one with a maximum temperature reduction of 0.9 °C and maximum temperature difference reduction of 1.17 °C at the inlet air flow rate of 60 L/s. Moreover, the cooling performance was further boosted by an aluminum heat spreader. The boosted design delivers an average Max T (32.95 °C) and an average ΔT (3.10 °C) at five different flow rates, which are 8.8% and 66.1% lower the one without the spreader (35.85 °C and 5.15 °C). Compared with the rectangular design without the spreader, the average Max T and ΔT of the boosted trapezoid design are reduced by 10.4% and 91.9% in addition to a space-saving of about 5.26%.

Keywords: electric vehicle; air cooling; battery thermal management system; trapezoid battery cell layout; aluminum heat spreader

Citation: Zhao, G.; Wang, X.; Negnevitsky, M.; Zhang, H.; Li, C. Performance Improvement of a Novel Trapezoid Air-Cooling Battery Thermal Management System for Electric Vehicles. *Sustainability* **2022**, *14*, 4975. https://doi.org/10.3390/su14094975

Academic Editor: Lin Li

Received: 15 March 2022
Accepted: 18 April 2022
Published: 21 April 2022

1. Introduction

Air pollution and global warming are regarded as two major threats to the sustainability of animals and human beings on our planet [1]. In recent years, electric transportation, especially electric vehicles (EVs) and hybrid electric vehicles (HEVs), has been playing a more and more critical role in the global green revolutions to tackle global warming and climate change issues [2]. In the recent decade, the rechargeable lithium-ion (Li-ion) battery packs have been the mainstream EV power supply sources due to their high power, superb reliability, and long lifespan [3]. With the rapid development of higher specific energy and lower manufacturing cost, the major problem of Li-ion batteries is shifting to its thermal management [4]. The abnormal heat dissipations and accumulations in the battery pack at high temperatures would adversely cause the battery accelerated degradation, capacity fading, and even thermal runaway accidents in some extreme cases [5]. At the moment, air cooling and liquid cooling are two major cooling methods for the battery thermal management system (BTMS) in commercial EVs [6]. Generally, the liquid-cooling BTMS is more favourable for its superior thermal exchangeability and compact design [7], but its manufacturing and maintenance costs are higher than the air-cooling BTMS. Lai et al. [8] proposed a compact and lightweight liquid-cooling BTMS with aluminum curved-surface thermal conductive structures. The novel design was proven to deliver excellent cooling efficiency. Tete et al. [9] reviewed most of the EV BTMS research in recent years, especially the

commercialized air and liquid-cooling techniques, and designed novel cylindrical casings for the liquid-cooling BTMS of cylindrical cells [10]. Moreover, Murali et al. [11] reviewed the studies about utilizing phase change materials as a cooling enhancement method to the hybrid BTMSs by the novel thermal conductivity increase techniques. However, the cost of these novel hybrid BTMSs are still high. Due to the fierce competitions in the global EV market, the cost reduction has been more and more important to the commercial success of any EV model. The extraordinary cost performance as well as excellent reliability of the air-cooling system has gained favors by many battery pack designers and automobile original equipment manufacturers (OEMs) including Nissan, PSA, SAIC, etc. [12]. Since the battery electrochemical and material technologies have been improved significantly [13], the internal heat generations of the Li-ion battery cells during charging and discharging are effectively suppressed, especially for some state-of-the-art battery technologies such as all-solid-state batteries [14]. Due to this technology upgrade of a lower cooling capacity demand trend from the EV OEMs, the air-cooling BTMS applications are presumably shifting from the mild heat generation ones such as HEVs to higher ones such as EVs [15]. In addition, its simple structure, superb reliability and cost-effective advantages made it a promising and competitive cooling method for the next generation EV accumulators [16].

As a typical thermal management (especially heat dissipation) device, the mechanisms of an air-cooling BTMS is similar to a heat exchanger [17]: transfer the heat from battery cells to the air flows. Although battery cells are not fluid, they can be treated as an entity of stable heat sources in the system. Theoretically, there are three major methods to improve the heat transfer efficiency: (1) increase the heat exchange coefficient [18]; (2) change the flow mode inside the fluid domain to increase the fullness of dimensionless parameters [19]; (3) enhance the degree of synergy between velocity field and temperature gradient field based on Field Synergy Principle (FSP) [20].

The second method can be implemented by changing the inlets/outlet positions and air flow channels. In this research, swapping the inlet/outlet positions of the trapezoid BTMS is based on this method. Some studies about the inlet/outlet and/or air flow channel improvements are briefly summarized in the following paragraph. Mahamud et al. [21] investigated the influence of a reciprocating flow design on the cooling performance of a rectangular layout battery pack. Compared with the one direction design, this design under a reciprocated air flow (reciprocation frequency = 120 s) effectively reduced the maximum temperature by 1.5 °C and the temperature difference by 4 °C. Na et al. [22] presented a reverse layered air-cooling BTMS of a rectangular battery pack of 2 × 10 38,120 cylindrical cells: a partition is placed in the horizontal middle plane within the battery pack to divide the cooling channel into two equal parts. The maximum average temperature difference was reduced by 47.6% (1.1 K). Chen et al. [23] developed a U-type air-cooling channel design for the parallel rectangular battery pack of 12 × 2 prismatic cells. The effect of plenum widths, angles, and inlet and outlet widths on the system performance was studied. The improved U-type design was proven to exhibit a 70% lower maximum temperature difference with a 32% power consumption reduction compared with the original U-type BTMS. Liu et al. [24] established a dynamic self-adapting J-type air-cooling BTMS with a rectangular battery pack of 1 × 10 prismatic cells. The J-type design was an integration of the conventional U-type and Z-type structures with an advanced adaptive control approach of the model predictive control strategy. The optimized design with mode switching control maintained the temperature difference at 1.33 K and improved the energy efficiency. Zhao et al. [25] adopted 18,650, 26,650, and 42,110 cylindrical cells in the rectangular designs with three types of inlets/outlets positions to compare the cooling performances. The influences of the inlet wind speed, gap spacing size, and the ambient temperature on the cooling performance of the BTMSs were investigated. Hong et al. [26] explored the suitable position and size of the secondary vent design on the original parallel rectangular battery pack of 12 × 2 prismatic cells. The results showed that adding the secondary vents on the outlet plenum reduced both 5 K maximum temperature and 60% maximum temperature difference compared with the designs without the secondary

vents. Zhang et al. [27] proposed a wedge-shaped layout air-cooling BTMS of a row of 12 parallel prismatic cells. The major parameters such as inlet/outlet position, flow path width, wedge angle, and cell clearance were optimized. The maximum temperature and average temperature of the 12° wedge-shaped design were 11.9 K and 1.5 K lower than the rectangular design in addition to a reduction of 224 Pa pressure difference.

The third method (FSP) can be regarded as the fundamental mechanisms of most cooling performance improvement methods. The heat generation of all the battery cells forms a temperature gradient field within the BTMS. To enhance the synergy degree between velocity field and temperature gradient field, both fields could be modified to form a smaller intersection angle between two fields [28]. Some studies focused on improving the temperature gradient field by changing the layout and/or spacing of the battery cells. The conventional rectangular layouts usually deliver poor synergy between two fields. Li et al. [29] adopted a wind tunnel to investigate the thermal performance of a rectangular battery pack of 4 × 8 cylindrical cells. Because the air flow is simply one direction from one short side of the rectangular to the other, a significant temperature gradient was observed along the air streamline. The intersection angle between temperature gradient field and air velocity field is almost 180°, indicating the poor fields synergy of the rectangular air-cooling BTMS. Wang et al. [30] explored five different cylindrical battery pack layouts: 1 × 24 rectangular, 3 × 8 rectangular, 5 × 5 rectangular, 19 hexagonal, and 28 circular arrangements. The results showed that the 5 × 5 rectangular layout with a top fan was the optimal design. Yang et al. [31] compared the thermal performances of aligned and staggered layouts of 10 × 6 cylindrical cells under a consistent air flow direction. The aligned layout design with specific longitudinal and transverse intervals (S_x = 34 mm, S_y = 32 mm) was selected as the optimal forced air-cooling system in the research. Chen et al. [32] optimized the battery cell spacings of a parallel rectangular battery pack of 12 × 2 prismatic cells. The results showed that the adjusted cell spacings remarkably reduced the maximum temperature difference by 42%. Chen et al. [33,34] investigated the influences of cell number and spacing distribution on the cooling performance of a typical parallel air-cooling BTMS with a rectangular battery pack of N × M prismatic cells. The maximum temperature and temperature difference were reduced by 4.0 K and 69% by the cell spacing optimization approach, and the maximum temperature and energy consumption were decreased by 43% and 33% by structural optimization designs.

Last but not least, the approaches of the first method include adding ribs, insertions, spoilers, and vortexes to improve the heat exchange coefficients by increasing the local Reynolds and Nusselt numbers. Because most of the auxiliary structures require extra space and cost, this research just added a simple aluminum heat spreader (AHS) after the optimizations of inlets/outlets positions and battery cells layout as a further improvement of the cooling efficiency without too much energy consumption increase. Xu et al. [35] adopted a thermally conductive aluminum double-layer heat spreading plate with anodized surfaces to improve the cooling performance of an air-cooling BTMS with a rectangular battery pack of 4 × 5 18,650 cylindrical cells. Some heat spreaders are specially designed for Li-ion battery pouch cells to enhance the cooling performance of forced air convection. Saw et al. [36] designed an aluminum metal foam as the heat spreader for $LiFePO_4$ pouch cells. The design was proved to maintain the maximum temperature below 35 °C and temperature difference below 5 °C. Wang et al. [37] also found that the open-cell aluminum foam spreaders between the Li-ion pouch cells could strengthen the thermal interactions between cells and reduce the temperature rise compared with the air cooling without aluminum spreaders; however, the foam structure also causes flow resistance and increase the power consumption.

Based on the above three fundamental heat transfer efficiency improvement methodologies, this research innovatively changed the conventional rectangular layout of the cylindrical battery cells to trapezoid one to acquire an effective temperature gradient field change. Synergizing with the change of a wide range of inlet velocities, the optimal cooling performance (presumably the highest degree of synergy between two fields) could be

obtained after exhaustive orthogonal simulations between different inlet and outlet size ratios (trapezoid base angles) and air flow rates. At the end of the research, a large-volume battery pack design consisting of multiple trapezoid battery packs with alternate inlets and outlets positions is presented for the commercial EV and HEV air-cooling BTMS.

2. 3D Modeling and Cooling Performance Indicators

2.1. Major Parameters and 3D Modeling of the Li-Ion 21700 Cylindrical Battery Cell

Li-ion 21,700 cylindrical battery cell is a recently developed type of commercial battery cell to provide higher energy density with lower manufacturing cost in comparison to the conventional 18,650 cell. The research about the 21,700 cells is relatively inadequate compared with those about the commercial 18,650 cylindrical, prismatic, and pouch cells. To fill this gap, this research focuses on the thermal performance of the 21,700 cell-based air-cooling BTMS. The major parameters of the Li-ion 21,700 cell are listed in Table 1. ANSYS Fluent software could automatically identify the numbers of the series or parallel configurations by the busbar connections based on the correct 3D battery pack modeling. The air is set as an incompressible ideal gas with viscosity as a function of temperature following Sutherland's Law.

Table 1. Li-ion 21,700 cylindrical cell major parameters.

Major Parameters	Values
Cell length (mm)	70
Cell diameter (mm)	21
Anode tab diameter (mm)	21
Anode tab height (mm)	5
Cathode tab diameter (mm)	13
Cathode tab height (mm)	5
Active material density (kg/m^3)	2092
Active material C_p (Specific Heat) (J/kg-K)	678
Active material thermal Conductivity (W/m-K)	18.2
Active material electrical Conductivity (Siemens/m)	3.541×10^7
Passive material density (kg/m^3)	8978
Passive material C_p (Specific Heat) (J/kg-K)	381
Passive material thermal Conductivity (W/m-K)	387.6
Passive material electrical Conductivity (Siemens/m)	1×10^7

To equalize the heat generations of each design, the cell quantities of the trapezoid and rectangular design are both 42. The trapezoid battery pack is shown in Figure 1a. The pack includes two rows of seven cells on one side, three rows of six cells in the middle, and two rows of five cells on the other side. In comparison, the conventional rectangular battery pack is shown in Figure 1b. The cell centre distance can be variable from 22 to 36 mm (cell surface distance from 1 to 15 mm) for the air-cooling BTMS of the cylindrical cells. From the previous research, the smaller distance usually increases the friction losses along the air channel at the same volumetric flow rate due to a higher air velocity, indicating a higher energy consumption [38]. The larger distance could not provide sufficient cooling performance due to low air velocity at the same air flow rate although it consumes less energy [3]. This research aims to balance the cooling performance and energy consumption and selects the medium value of 30 mm following some published air-cooling BTMS studies [39–41]. The vertical distance between the cell centres of two staggered columns in the trapezoid design is 15 mm, which is also the unified vertical distance between staggered columns in all derivative trapezoid designs in this research.

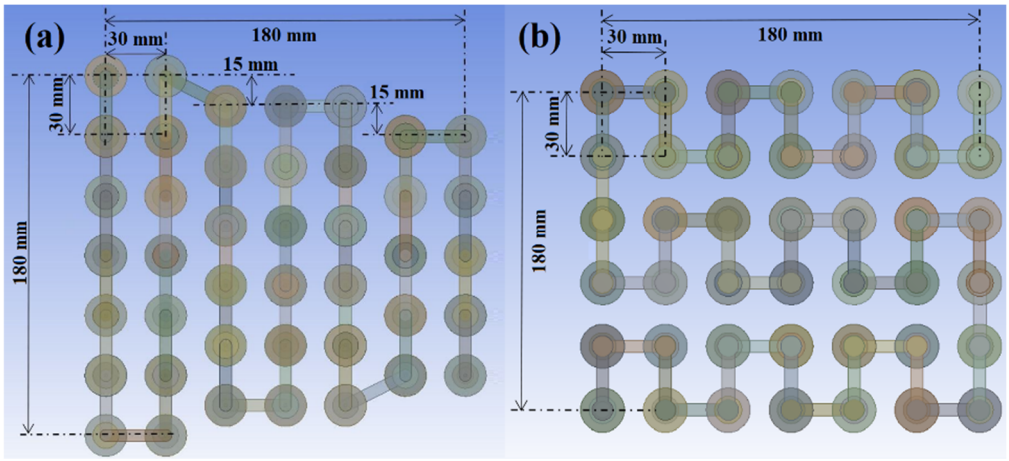

Figure 1. Battery pack layouts and dimensions: (**a**) Novel trapezoid design; (**b**) Conventional rectangular design.

2.2. Cooling Performance Indicators and Evaluation Criteria

From the literature reviews in the first section, maximum temperature (Max T), minimum temperature (Min T), and maximum temperature difference (ΔT) are mostly used to evaluate the overall cooling performances, while maximum pressure difference (ΔP) is usually used to indicate the power consumption of the air-cooling BTMS. In this research, these four indicators are all adopted to evaluate the overall performance. Max T/Min T refer to the maximum/minimum temperatures on the surfaces of all cells and busbars during the whole discharging process. ΔT is the maximum difference between Max T and Min T at any time during the whole discharging process. According to the Li-ion battery cell electrochemical model, the battery heat generation rate is usually highest at the end of the discharging process which the Max T is achieved at the end of the discharging, so the ΔT values in this research are mostly the values at the last time step of the discharging simulation. ΔP is the difference between the inlet average pressure and outlet average pressure at the end of the discharging process. Because ΔP is more like a constant value during the whole discharging process which is only dependent on the inlet velocity values and BTMS intrinsic structures, the ΔP values in this research are also recorded at the last time step of the simulation.

Basically, the ideal operating temperature range for Li-ion batteries is between 25 °C (298.15 K) and 40 °C (313.15 K) [42–47]. The overheat of battery cells would lead to accelerated degradation, capacity fading, or even full damage of the cells [48]. Due to the deviations of the temperature control accuracy of EV BTMS (around ±1 K) and the high power output requirement of the commercial EVs (more uniform cell temperatures could deliver more stable and accurate power output since the battery output performance is significantly related to the battery temperature [49]), the maximum Li-ion battery cell operating temperature should be close to 25 °C to deliver the best output performance and maintain the longest service lifetime [50,51]. Although 25 °C is the ideal operating temperature for Li-ion batteries, the cooling capacities of both active and passive air-cooling BTMSs heavily rely on the ambient temperatures. The ambient and inlet air temperatures are initially set as 20 °C (293.15 K) in this research to obtain the optimal design. Due to the limited difference (5 K) between ambient temperature (293.15 K) and ideal operating temperature (298.15 K), it is almost impossible for an active air-cooling BTMS to maintain the maximum operating temperature under 25 °C during a medium or above discharging process (≥1 C). As one of the two cooling performance evaluation criteria in this research, 35 °C (308.15 K) is chosen as the upper threshold of the Max T values to offer a reasonable temperature control buffer (10 K) for the air-cooling BTMS. For the other criterion, the upper threshold of the ΔT values is selected as 5 K, which is widely elucidated by much other research [8,52–57].

3. Mathematical Models and Validations

To simulate both Li-ion battery cell heat generation and forced air-cooling processes, this research couples two models in the ANSYS Fluent: (1) battery electrochemical model to predict the heat generations from the electrochemical reactions inside the cells during discharging; (2) heat and mass transfer model to simulate the cooling performances of the forced air-cooling process.

3.1. Battery Electrochemical Model

The dual-potential multi-scale multi-domain (MSMD) battery simulation approach and electric circuit model (ECM) are adopted as the major simulation methodologies in ANSYS for the battery cell heat generation predictions. Newman's electrochemistry model is simplified in Equation (1) to calculate the electric potentials [58]:

$$\int_V \nabla \cdot (\sigma \nabla \varnothing) dV = \int_A j dA \tag{1}$$

where ∇ is the Del operator which denotes a partial derivative of a quantity with respect to all directions in the chosen coordinate system, ϕ is the electric potential, j is the volumetric transfer current density, A is the surface area of the interface, σ is the electrical conductivity.

The dual-potential MSMD approach is specially designed for the study of the thermal and electrochemical behaviour of the multiple Li-ion battery cells system. The electrical and thermal fields of the battery cells could be expressed by Equations (2)–(4) [59]:

$$\frac{\partial \rho C_p T}{\partial t} - \nabla \cdot (k \nabla T) = \dot{q} \tag{2}$$

$$\nabla \cdot (\sigma_+ \nabla \varphi_+) = -j \tag{3}$$

$$\nabla \cdot (\sigma_- \nabla \varphi_-) = j \tag{4}$$

where ρ is the mass density of the battery cell, C_p is the specific heat capacity of the battery cell, T is the temperature, k is the thermal conductivity, q is the heat generation rate which consists of the Joule heat, the electrochemical reaction heat, and the entropic heat, σ_+ and σ_- are the anode and cathode effective electrical conductivities, φ_+ and φ_- are the anode and cathode phase potentials.

For the ECM interpretations, a diagram of a six-parameter circuit model including three resistors and two capacitors is proposed by Chen et al. [60] to simulate Li-ion battery cell internal electrochemical behaviour in Figure 2.

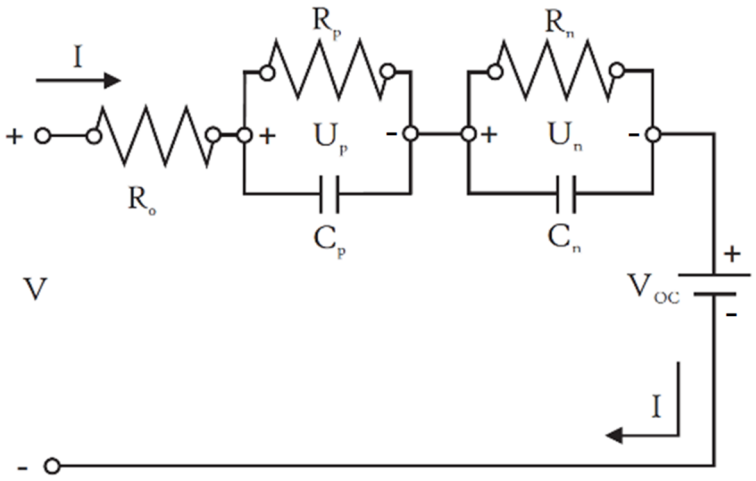

Figure 2. ECM diagram for Li-ion battery.

In the ECM, the relations between voltages and currents are expressed in Equations (5)–(8):

$$V(t) = V_{OC}(SoC) + V_p + V_n - R_o(SoC)I(t) \tag{5}$$

$$\frac{dU_p}{dt} = -\frac{1}{R_p(SoC)C_p(SoC)}V_p - \frac{1}{C_p(SoC)}I(t) \tag{6}$$

$$\frac{dU_n}{dt} = -\frac{1}{R_n(SoC)C_n(SoC)}V_n - \frac{1}{C_n(SoC)}I(t) \tag{7}$$

$$\frac{d(SoC)}{dt} = \frac{I(t)}{3600Q_{Ah}} \tag{8}$$

where V is the battery voltage, I is the battery current, V_{OC} is the open-circuit voltage, SoC is the state of charge, V_p and V_n are the voltages of R_p/C_p and R_n/C_n, R_o, R_p and R_n are the resistance of resistor o, p, and n, C_p and C_n are the capacitance of capacitor p and n, Q_{Ah} is the total battery capacity.

Chen et al. [60] found that the open-circuit voltage (V_{OC}), series resistors (R_o), and RC network (R_p, C_p, R_n, and C_n) are all SoC-dependent parameters and independent of discharge currents. The following single-variable Equations (9)–(14) are used to solve the above equation set:

$$R_o = a_0 e^{a_1(SoC)} + a_2 \tag{9}$$

$$R_p = b_0 e^{b_1(SoC)} + b_2 \tag{10}$$

$$C_p = c_0 e^{c_1(SoC)} + c_2 \tag{11}$$

$$R_n = d_0 e^{d_1(SoC)} + d_2 \tag{12}$$

$$C_n = e_0 e^{e_1(SoC)} + e_2 \tag{13}$$

$$V_{OC} = f_0 + f_1(SoC) + f_2(SoC)^2 + f_3(SoC)^3 + f_4(SoC)^4 + f_5(SoC)^5 \tag{14}$$

where a_n, b_n, c_n, d_n, e_n, and f_n (n = 0, 1, . . . , 5) are the constant coefficients.

The key ECM parameters, including nominal cell capacity, specified C-Rate, Max and Min stop voltages, initial SoC, reference capacity, and all the constant coefficients are listed in Table 2.

Table 2. Key ECM Parameters.

Battery ECM Parameters	Values
Nominal Cell Capacity (Ah)	4
Specified C-Rate	1
Max Stop Voltage (V)	4.3
Min Stop Voltage (V)	3
Initial SoC	1
Reference Capacity (Ah)	4
a_0	0.07446
a_1	0.1562
a_2	24.37
b_0	0.04669
b_1	0.3208
b_2	29.14
c_0	703.6
c_1	−752.9
c_2	13.51
d_0	0.04984
d_1	6.603
d_2	155.2
e_0	4475
e_1	−6056
e_2	27.12
f_0	3.685
f_1	0.2156
f_2	−0.1178
f_3	0.3201
f_4	−1.031
f_5	35

3.2. Thermodynamic Model

In the ANSYS Fluent, the thermodynamic model is based on three fundamental conservation equations: mass, momentum, and energy conservation equations. The mass conservation equation for the incompressible ideal gas air flows is expressed by Equation (15) [61]:

$$\frac{\partial \rho}{\partial t} + \nabla \cdot \left(\rho \vec{v} \right) = 0 \tag{15}$$

where ρ is the air mass density, $\vec{v}$ is the air flow velocity vector.

The momentum conservation in an inertial reference frame is expressed by Equation (16) [62]:

$$\frac{\partial \left(\rho \vec{v} \right)}{\partial \mathrm{t}} + \nabla \cdot \left(\rho \vec{v} \vec{v} \right) = -\nabla p + \nabla \cdot \left(\bar{\bar{\tau}} \right) \tag{16}$$

where p is the static pressure, $\bar{\bar{\tau}}$ is the stress tensor.

The general energy conservation equation is expressed in Equation (17) [63]:

$$\frac{\partial \left(\rho C_p T \right)}{\partial t} + \nabla \cdot \left(\vec{v} (\rho T + p) \right) = k \nabla^2 T + q_b \tag{17}$$

where C_p is the specific heat capacity of the air, p is the pressure, k is the thermal conductivity, q_b is the battery heat generation rate.

3.3. Mesh Independence Test and Model Validation

The mesh independence test is conducted to determine the optimal mesh sizes. From Table 2, the Max and Min stop voltages are set as 4.3 V and 3 V. Because the output voltage of the battery cell will decrease with the drop of the SoC, the simulation will automatically cease when the output voltage drops to 3 V. For a 3D model of a single 21,700 cylindrical cell, the simulation results of the mesh sizes of 25 × 50 (division number of Anode tab diameter × division number of Cathode tab diameter), 50 × 100, and 80 × 160 during 0.3 C, 0.6 C, and 1 C discharging operations are compared separately. The difference of the temperature prediction values under three different mesh sizes are almost neglectable (less than 0.1%). To save the calculation time and optimize the simulation efficiency, the mesh size 25 × 50 will be adopted in this research.

The ECM battery cell and heat transfer models are validated by comparing the simulation results with the experimental data in reference research by Fan et al. [38] of an air-cooling BTMS with a rectangular battery pack of 4 × 8 18,650 cylindrical cells in an acrylic wind tunnel in Figure 3a. Every four cells in the column are connected in parallel, and the eight columns are connected in series following a 4p8s connection. The reference experiments are conducted at inlet flow rates of 0.6 m/s, 1 m/s, 2 m/s, 3 m/s, and 4 m/s. Figure 3b shows the 3D validation model. The cell centre distance is 22 mm. The distance between the cell centre and the acrylic wall is 13 mm. The inlet air temperature and the ambient temperature are 20 °C. The discharge rates are 0.5 C, 1 C, and 2 C.

Figure 4a shows the temperature contour and air velocity streamlines at 4 m/s 20 °C inlet air during 0.5 C discharging. Figure 4b shows the comparison between the experimental data and the simulation results during 0.5 C, 1 C, and 2 C discharging. The average errors between experimental and simulation results at five different velocities during 0.5 C, 1 C, and 2 C discharging are 0.12 K, 0.47 K, and 0.37 K, respectively. The standard deviations of the errors between experimental and validation values at five different velocities during 0.5 C, 1 C, and 2 C discharging are 0.35 K, 0.94 K, and 0.33 K, respectively. These comparison results indicated that the simulation model is accurate and reliable to be used to predict the thermal performance of air-cooling BTMSs. The relatively large error points in the simulation might be the results of the experimental measurement errors as reported in the reference paper.

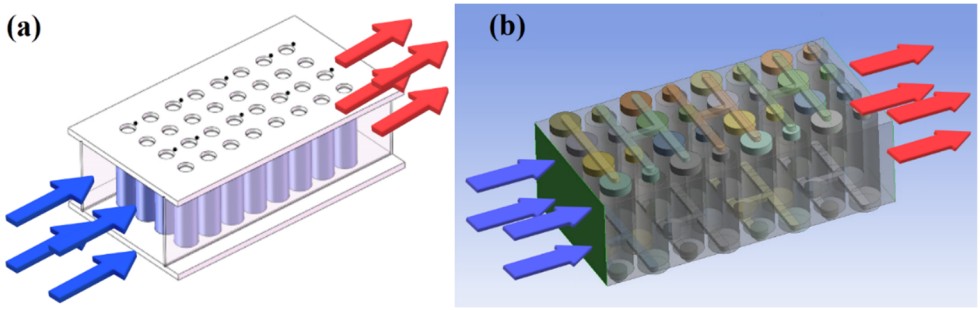

Figure 3. Model validation: (**a**) Reference experimental set up (Ref. [38]); (**b**) 3D validation model in this research.

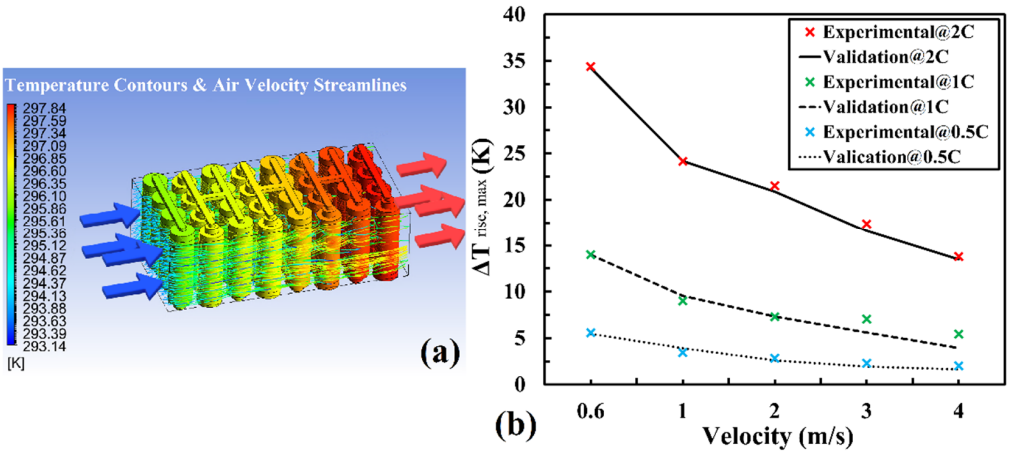

Figure 4. Validation results: (**a**) Temperature contours and air velocity streamlines at 4 m/s 20 °C inlet air during 0.5 C discharging; (**b**) Comparison between the experimental data in Ref. [38] and the validation results in this research.

4. Results and Analysis

The simulation works in this research include four objectives: (1) comparison between conventional rectangular design and novel trapezoid design; (2) optimization of inlet/outlet positions of the trapezoid design; (3) optimization of the base angles of the trapezoid design; (4) the cooling effects of an additional single-layer AHS.

4.1. Comparison between Conventional Rectangular and Novel Trapezoid Designs

The first objective is to evaluate the performance of the novel trapezoid design in comparison to the conventional rectangular design. Figure 5 shows the 3D models of the trapezoid air-cooling BTMS design (seven-cell-base inlet) and the rectangular counterpart (six-cell-side inlet).

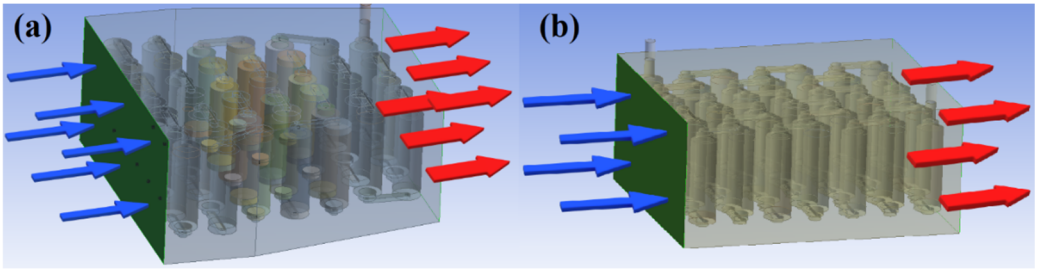

Figure 5. Air-cooling BTMS: (**a**) Trapezoid design; (**b**) Rectangular design.

The simulations are conducted at the five different flow rates (20 L/s, 40 L/s, 60 L/s, 80 L/s, and 100 L/s). Because the inlet size of the trapezoid design (0.022 m^2) is larger than the rectangular one (0.02 m^2), the inlet velocities of the trapezoid design will be decreased to deliver the same flow rates as those in the rectangular design. Table 3 lists the corresponding inlet velocities and dimensions for Rectangular design (Design R) and Trapezoid design (Design T) at five different flow rates.

Table 3. Rectangular (R) and Trapezoid (T) BTMS.

Design No.	Inlet Velocity (m/s)	Inlet Dimension (m)	Volume Air Flow Rate (L/s)	Mass Air Flow Rate (g/s)	Outlet Dimension (m)
R-1	1	0.1 m × 0.2 m 6-cell-side inlet	20	23.98	0.1 m × 0.2 m 6-cell-side outlet
R-2	2		40	47.96	
R-3	3		60	71.94	
R-4	4		80	95.92	
R-5	5		100	119.90	
T-1	0.91	0.1 m × 0.22 m 7-cell-base inlet	20	23.98	0.1 m × 0.16 m 5-cell-base outlet
T-2	1.82		40	47.96	
T-3	2.73		60	71.94	
T-4	3.64		80	95.92	
T-5	4.55		100	119.90	

Figure 6 shows the simulation results of both designs at five different flow rates. The Max T values of Design T are lower than those of Design R at flow rates from 20 to 80 L/s while the Min T values of Design T are higher than those of Design R. This leads to an advantage of the temperature uniformity performance of the trapezoid design. From the FSP, the direction of the temperature gradient field of the trapezoid design is from the seven-cell-base inlet to the five-cell-base outlet (the side with more cell numbers in one column is presumably the side with higher temperature), which completely conforms to the direction of the air flow velocity field (from seven-cell-base inlet to the five-cell-base outlet). The coincidence leads to an almost zero-degree intersection angle between two fields, leading to a better cooling performance than the rectangular design. Moreover, the temperature difference of the trapezoid design is also smaller from 20 to 80 L/s. When the flow rate is increased to 40 L/s, Design T firstly meets the evaluation criterion of ΔT (4.31 K < 5 K), while Design R meets the same criterion (4.25 K < 5 K) when the flow rate is 80 L/s. A 50% reduction in the cooling air flow rate and a nearly 70% reduction in ΔP (ΔP of Design T at 40 L/s is 18.05 Pa and ΔP of Design R at 80 L/s is 59.14 Pa) is a superior indication of less energy consumption. Although Design R shows a lower pressure drop than Design T at the same inlet flow rate, the maximum temperature differences of Design T are much lower than Design R at close pressure drops.

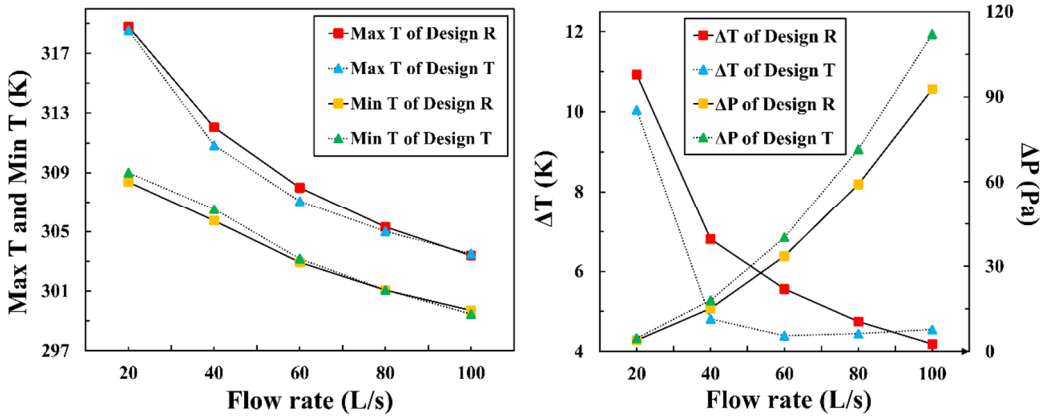

Figure 6. Simulation results of Design R and Design T at five different flow rates.

Figure 7 shows the temperature contours on the middle plane of Design T at five different flow rates. As the flow rate increases, the hot spot regions of the cells move from the areas near the outlet to the inlet, revealing a direction change of the temperature gradient field. The reversed temperature gradient field gradually conforms to the velocity field (the intersection angle between temperature gradient field and velocity field gradually changes from 180° to 0°), leading to a better cooling efficiency and performance following the FSP. The width of the colour range indicates the level of the temperature uniformity of the battery pack cells. It is found that the colour ranges of the Design T at 40 L/s, 60 L/s, 80 L/s and 100 L/s are relatively narrow and their corresponding ΔT are 4.31 K, 3.89 K, 3.95 K, and 4.05 K, respectively. The Max T value at 40 L/s (310.84 K) is also lower than the evaluation criterion of Max T 308.15 K. Thus, the trapezoid design is a qualified design at a flow rate of 40 L/s.

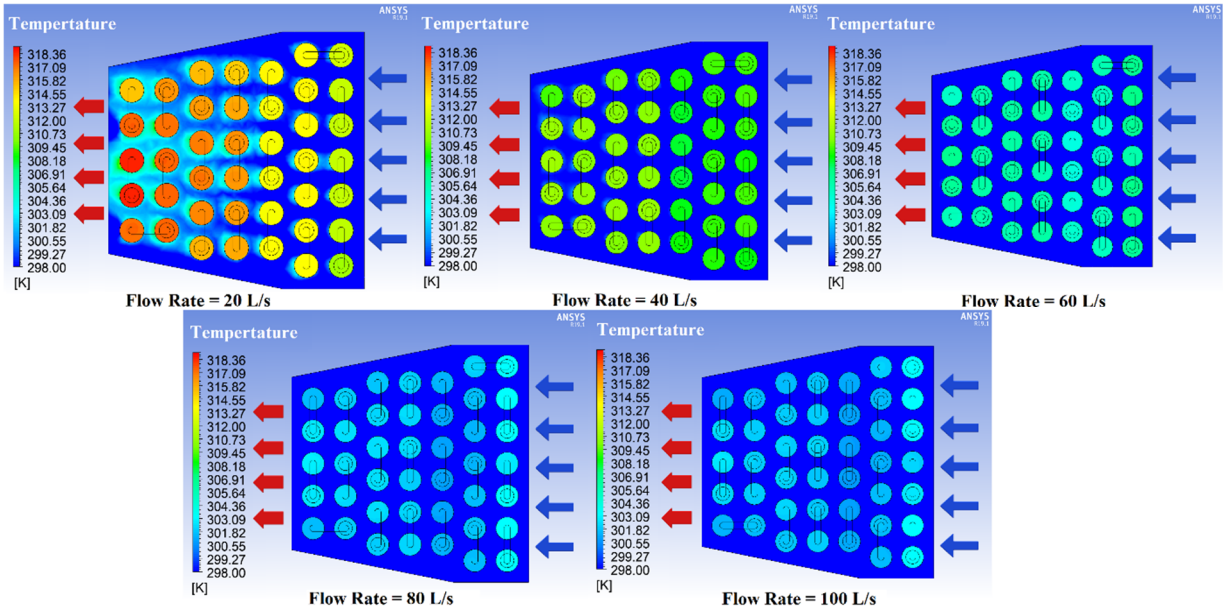

Figure 7. Temperature contours of Design T at five different flow rates.

4.2. Cooling Effects of Air Flow Directions on Trapezoid Design

The first section of simulations successfully proves the better cooling performance of the trapezoid design than the rectangular one. In this section, the effect of the flow direction on the cooling performance of the trapezoid design will be investigated. Unlike the rectangular design whose inlet and outlet are identical, the trapezoid design has a pair of asymmetrical sides (seven-cell-base side and five-cell-base side). The inlet on the different sides is supposed to deliver different cooling performances. The simulations at five different flow rates (22 L/s, 44 L/s, 66 L/s, 88 L/s, and 110 L/s) with a seven-cell-base inlet (Large inlet) are grouped as Design L and the ones with a five-cell-base inlet (Small inlet) are grouped as Design S. To make a fair comparison, the five flow rates of two groups are kept as same. Table 4 shows the comparison working conditions.

Table 4. Large inlet (L) and Small inlet (S) trapezoid BTMS.

Design No.	Inlet Velocity (m/s)	Inlet Dimension	Volume Air Flow Rate (L/s)	Mass Air Flow Rate (g/s)	Outlet Dimension (m)
L-1	1	0.1 m × 0.22 m 7-cell-base inlet	22	26.38	0.1 m × 0.16 m 5-cell-base outlet
L-2	2		44	52.76	
L-3	3		66	79.14	
L-4	4		88	105.52	
L-5	5		110	131.90	
S-1	1.375	0.1 m × 0.16 m 5-cell-base inlet	22	26.38	0.1 m × 0.22 m 7-cell-base outlet
S-2	2.750		44	52.76	
S-3	4.125		66	79.14	
S-4	5.500		88	105.52	
S-5	6.875		110	131.90	

Figure 8 shows the simulation results of the Max T, Min T, ΔT, and ΔP values of the trapezoid design in two groups. The Max T values in Design L are always lower than Design S while the Min T values in Design L are higher than Design S, leading to a better temperature uniformity (small ΔT) of Design L. This is because the Max T often occurred at the allocation close to the end of the flow channel due to the air flow direction. When the following channel cross-section area is growing smaller in Design L, the cooling air velocity increases and hence enhances the heat transfer coefficient. In Figure 9, the poor temperature uniformity of Design S at both 22 L/s and 110 L/s can also be explained by FSP: even if the flow rate increased from 22 L/s to 110 L/s, the variable air flow velocities still could not turn the direction of temperature gradient field reversely from "outlet → Inlet" to "inlet → outlet", keeping the intersection angle between velocity field (from inlet to outlet) and temperature gradient field (from the higher outlet side to the lower inlet side) being 180°, which is almost the worst degree of the synergy between two fields. Although the pressure drop in Design L is slightly higher than that in Design S, it is worthwhile because the cooling performance of Design L is much better than that of Design S at similar pressure drop scenarios.

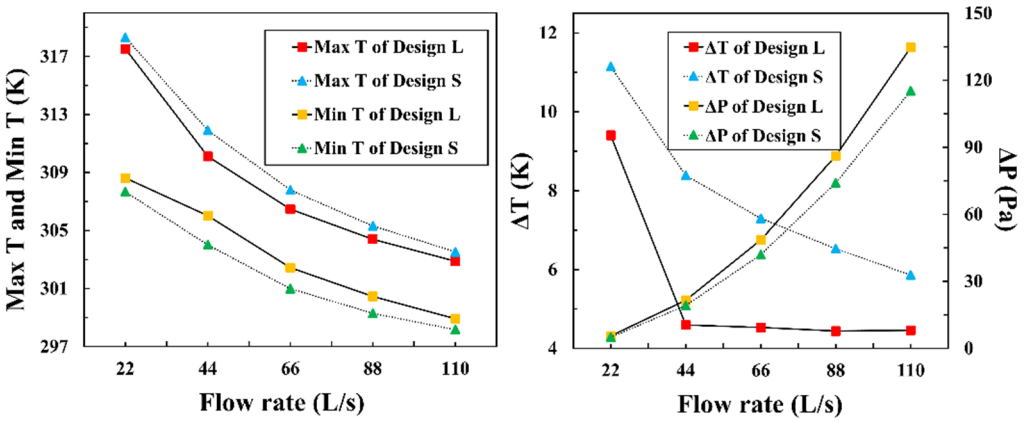

Figure 8. Simulation results of Design L and Design S at five different flow rates.

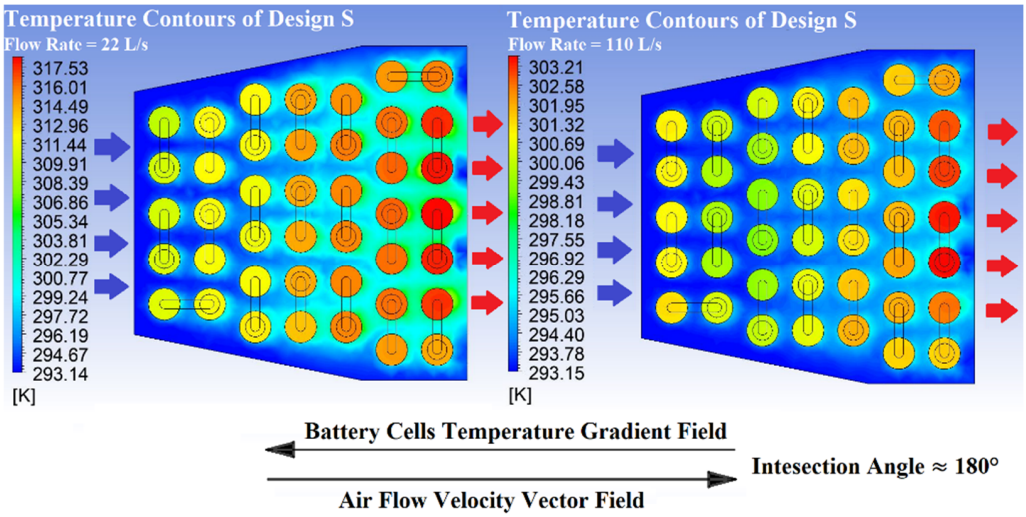

Figure 9. Temperature contours of Design S at 22 L/s and 110 L/s.

4.3. Trapezoid BTMS Design Optimization

From the second part of the simulations, the direction of the cooling air from the larger inlet to the smaller outlet could achieve better cooling performance for the trapezoid BTMS design. Because the ratio of the longer and shorter bases of different trapezoids can be different, the next step is to investigate the optimal ratio of the short base (outlet) to the long base (inlet). The base angle of the isosceles trapezoid can also be used to express the ratio of the short base to the long base. In this research, a smaller base angle means a smaller ratio of the outlet size to the inlet size. In this section, two more trapezoid BTMSs are presented to be inspected: eight-cell-base inlet with four-cell-base outlet design in Figure 10a and nine-cell-base inlet with three-cell-base outlet design in Figure 10b. The cell centre distances are 30 mm. The vertical distances of the cell centres of two staggered cell columns are 15 mm.

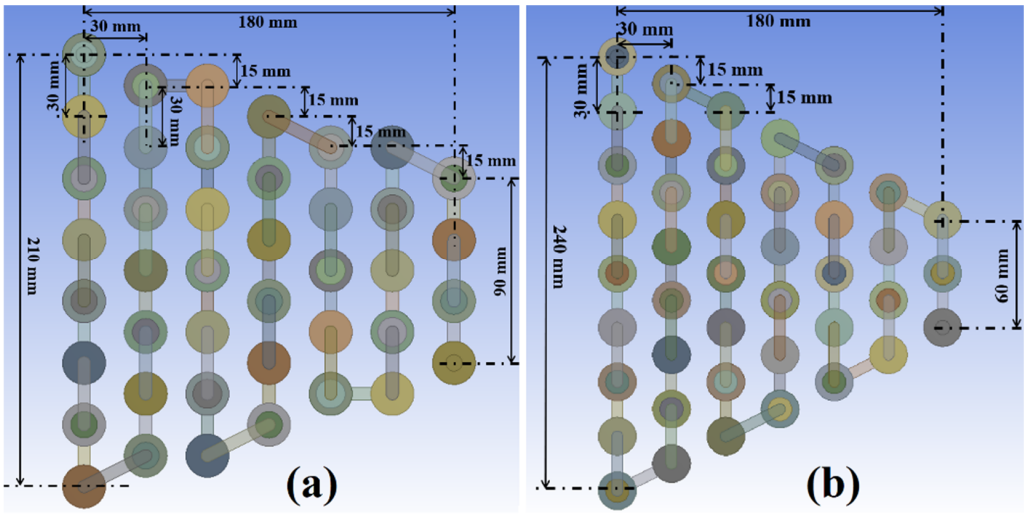

Figure 10. Trapezoid BTMS: (**a**) eight-cell-base inlet design; (**b**) nine-cell-base inlet design.

To comprehensively compare the cooling performances of the trapezoid designs with different base angles, the simulation results of two new trapezoid designs (eight-cell-base inlet design and nine-cell-base inlet design) are compared with the two designs in Section 4.1 (six-cell-base inlet rectangular design and seven-cell-base inlet trapezoid design). The rectangular design can be regarded as a special 90° base angle trapezoid design (six-cell-side inlet). The geometrical parameters of the four trapezoid designs are listed in Table 5.

Table 5. The geometrical parameters of four trapezoid BTMS.

Design No.	Inlet Descriptions	Long Base Length (m)	Short Base Length (m)	Height (m)	Base Angle (°)	Ratio of Short Base (Outlet) to Long Base (Inlet)
6	6-cell-side inlet (Rectangular)	0.2000	0.2000	0.2200	90.00	1.00
7	7-cell-base inlet (Trapezoid)	0.2200	0.1600	0.2200	78.69	0.73
8	8-cell-base inlet (Trapezoid)	0.2500	0.1300	0.2200	74.75	0.52
9	9-cell-base inlet (Trapezoid)	0.2935	0.0735	0.2200	63.44	0.25

Figure 11 shows the Max T, Min T, ΔT, and ΔP values of four trapezoid designs at five different flow rates (20 L/s, 40 L/s, 60 L/s, 80 L/s, and 100 L/s). All four designs meet the Max T criterion (<308.15 K) when the flow rate is increased to 60 L/s. Meanwhile, only Design 7 (3.89 K) and Design 8 (4.98 K) meet the ΔT criterion (<5 K) at 60 L/s. Because the Max T of Design 7 (307.07 K) and Design 8 (307.28 K) are quite close to each other, Design 7 is the optimal design at 60 L/s due to its better temperature uniformity performance. Figure 12 shows the temperature contours on seven cross-section planes of Design 7 at 60 L/s. The temperature distribution is quite uniform, and the dominant colour range is narrowly clustered between dark orange and red on a rainbow spectrum. The temperature gradient field complies with the velocity field in high consistency, indicating a perfect synergy of two fields and a favourable heat transfer coefficient of the system. At 60 L/s, with the decrease of the base angles, the quick drop of Min T values adversely causes the increase of ΔT values of Design 8 and Design 9 (especially Design 9 with the smallest base angle). Furthermore, the pressure drops in Design 8 and Design 9 increase remarkably with the increase in the flow rates, showing an exponential rise in power consumption. At 80 L/s and 100 L/s, although all the designs could deliver qualified Max T values, the ΔT values of Design 8 and Design 9 continue to exceed the criterion (5 K). As a result, Design 7 is selected as the optimal design among this simulation group.

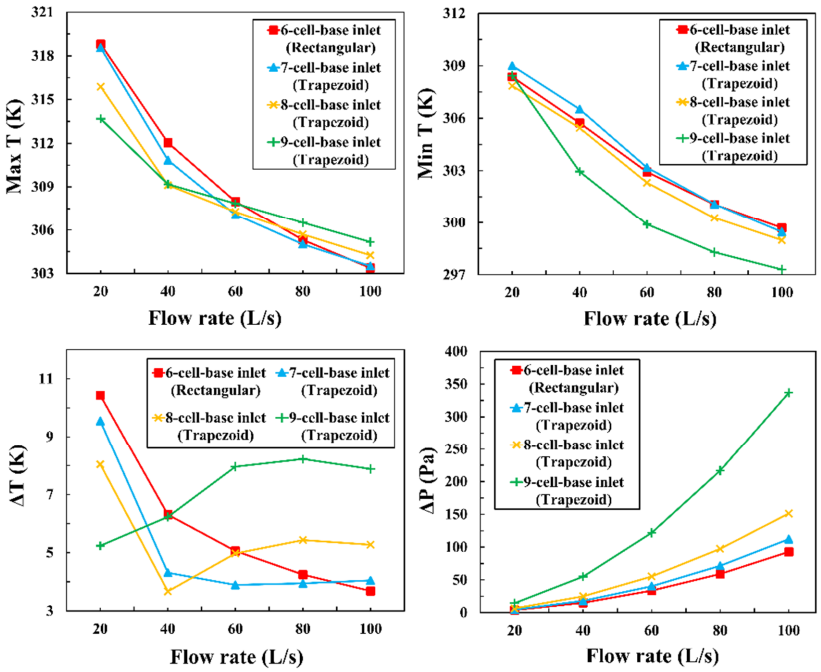

Figure 11. Simulation results of four trapezoid designs at different flow rates.

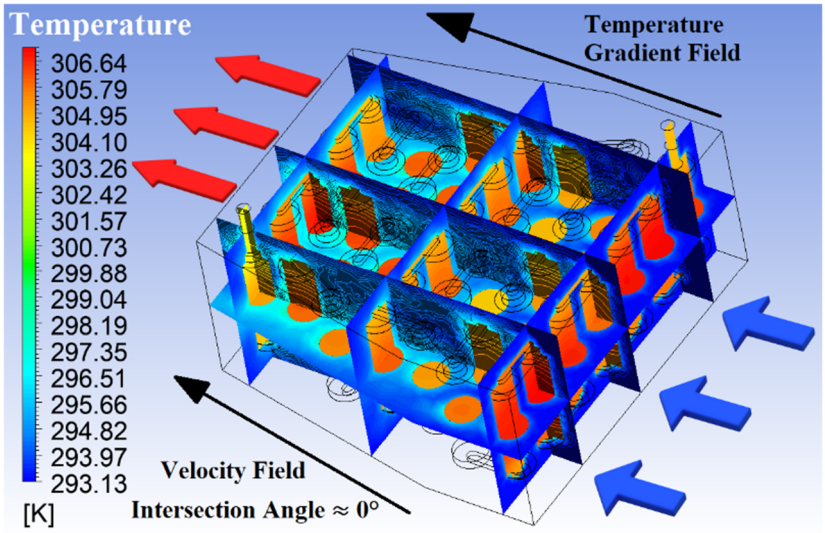

Figure 12. Temperature contours on seven cross-section planes of Design 7 at 60 L/s.

4.4. Cooling Effect of a Single-Layer AHS

To increase the stiffness and rigidity of the battery pack, the cylindrical cells are usually held and protected by two layers of plastic plates on both sides of the cells. In this research, a single-layer AHS is installed on the middle plane to enhance the overall strength of the battery pack as shown in Figure 13. More importantly, the AHS can be used as an auxiliary component to increase the heat exchange coefficient due to the high thermal conductivity and low volumetric mass density of aluminum. The thickness of the plate is 3 mm. The plate has complete contact to the middle cell surfaces with a total contact area of 197.92 mm^2. The specific heat and thermal conductivity of the aluminum is 871 $J \cdot kg^{-1} \cdot K^{-1}$ and 202.4 $W \cdot m^{-1} \cdot K^{-1}$, respectively. The three major purposes of adding the AHS are as follows: (1) to strengthen the stiffness and rigidity of the battery pack; (2) to help to evenly distribute the heat unevenly generated and accumulated on different cells; (3) to increase the heat exchange surface areas between the cells and the air flow. The total contact areas between air flow domain and cell surfaces increase from 193,961.93 mm^2 (total surface areas of 42 cells) to 239,615.28 mm^2 (total surface areas of the sum of 42 cells and AHS) by about 19%.

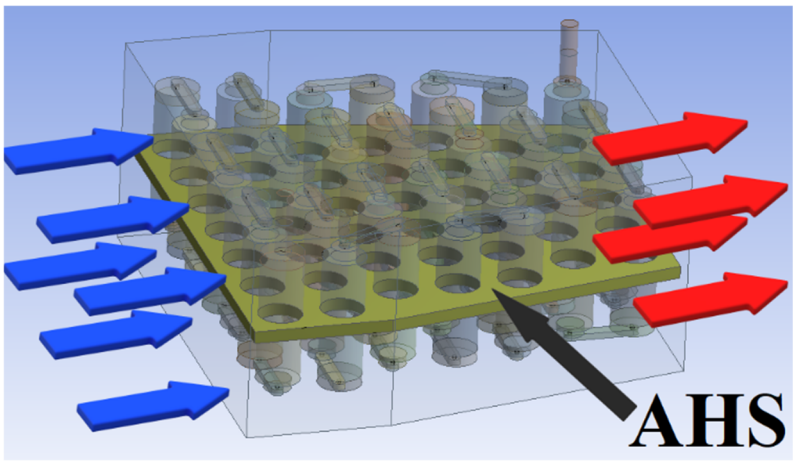

Figure 13. The optimal trapezoid design with a single-layer AHS.

Figure 14 shows the Max T, Min T, ΔT, and ΔP values of the optimal trapezoid design with and without a single-layer AHS at five different flow rates. The cooling performance improvement by adding the AHS is remarkable: (1) the Max T values of the design with

the AHS are 4.60 K, 2.58 K, 2.34 K, 2.48 K, and 2.48 K lower than those without the AHS at the flow rates of 20 L/s, 40 L/s, 60 L/s, 80 L/s, and 100 L/s, respectively; (2) the ΔT values of the design with the AHS are 3.78 K, 0.77 K, 1.52 K, 1.97 K, and 2.21 K lower than those without the AHS at five flow rates, respectively. Although both designs meet the ΔT criterion (<5 K) at 40 L/s, neither of the two designs meets the Max T criterion (<308.15 K) at 40 L/s. However, the Max T of the AHS design (308.26 K) is only 0.11 K over the upper threshold at 40 L/s. As a result, the trapezoid design with the AHS at 60 L/s is regarded as the optimal design delivering satisfied Max T and ΔT values of 2.34 K and 1.52 K lower than the design without the AHS at the cost of only a slight ΔP increase of 6.43 Pa. The simulation results proved the effectiveness of AHS to further improve the cooling performance of the trapezoid BTMS with less air flow rate.

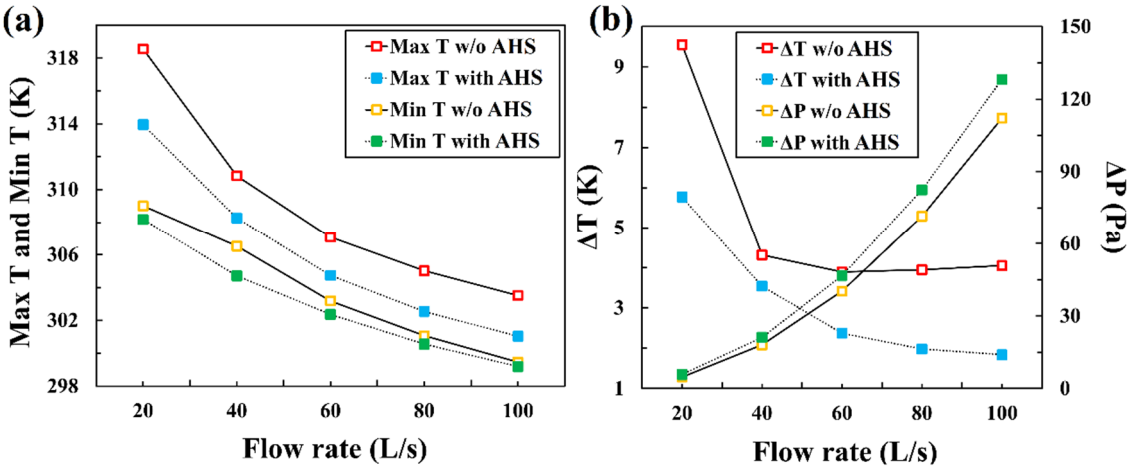

Figure 14. The simulation results of the optimal trapezoid design with and without a single-layer AHS at five different flow rates: (**a**) Max T and Min T; (**b**) ΔT and ΔP.

5. Discussion

The seven-cell-base inlet trapezoid design could effectively enhance the cooling performances of the air-cooling BTMS compared with the rectangular (six-cell-side inlet) design and smaller base angle trapezoid designs (eight-cell-base inlet design and nine-cell-base inlet design). With the help of a single-layer AHS, its cooling performance could be further improved. Thus, the novel trapezoid design is strongly recommended to be adopted in the commercial EV air-cooling BTMS applications. For example, Figure 15 shows a battery module of 84 pieces of cylindrical 21,700 cells. The layout of battery cells can be rearranged into a novel trapezoid one in Figure 15b from the conventional rectangular one in Figure 15a. The total area of the rectangular pack is 0.0836 m^2 while the total area of the trapezoid one is 0.0792 m^2. Compared with the rectangular design, the trapezoid one with a single-layer AHS not only saves about 5.26% space but also improves the overall cooling performances by a 10.4% decrease in Max T and a 91.9% decrease in ΔT. Furthermore, if the manufacturers do not want to change the structure in the EVs due to the space concern, the trapezoid could be achieved by simply adding some additional thin-wall partitions through the clearances between the cells within the original modular battery packs.

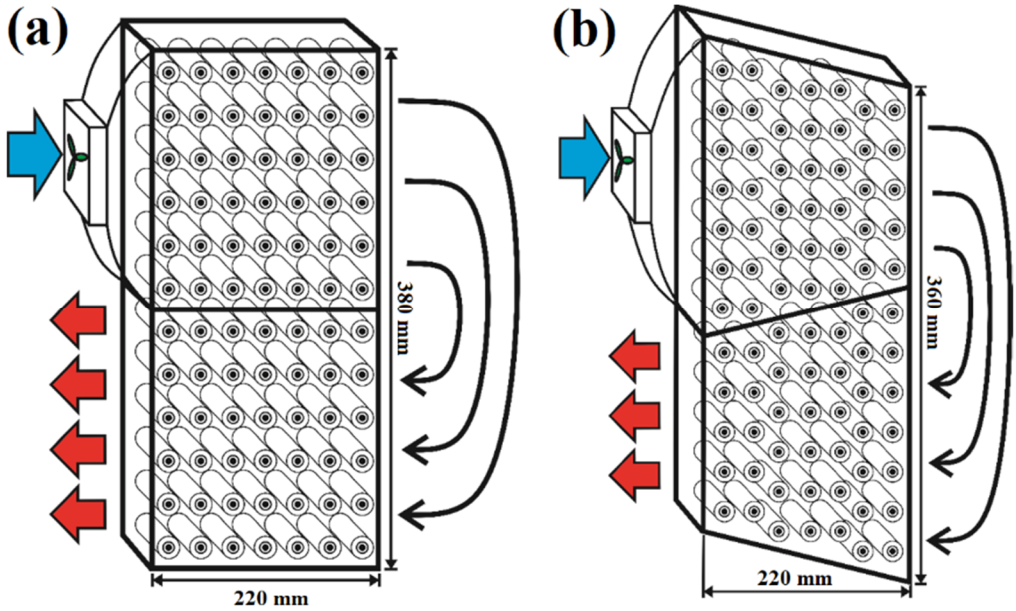

Figure 15. Air-cooling BTMS: (**a**) Conventional rectangular battery pack; (**b**) Novel trapezoid battery pack.

6. Conclusions

This research proposed a novel trapezoid air-cooling BTMS to deliver better cooling performances with less space requirement and almost no additional manufacturing cost. The mathematical battery heat generation model as well as the heat and mass transfer model are validated and applied to evaluate the cooling performance of the novel trapezoid design with an additional AHS. The optimal trapezoid base angle is figured out with the support of both the simulation results and the theoretical analysis based on the FSP. Some conclusions about the design optimization research are drawn below:

- The air flow direction has a dominant impact on the cooling performance of the trapezoid BTMS. Based on the FSP, the air flow velocity vector field should be consistent with the battery cells temperature gradient field to form a 0° intersection angle between two fields. A smaller synergy intersection angle usually leads to higher heat transfer coefficient. Since the high-temperature profile of the trapezoid design is on the long-base side and low-temperature profile is on the short-base side, the direction of the temperature gradient field is always from the long base to the short base if the boundary condition keeps constant. Thus, the velocity field should also be imposed along the direction of the temperature gradient field—from the long-base side to the short-base side, i.e., the inlet on the long-base side and the outlet on the short-base side for the trapezoid design.
- In this research, the optimal base angle of the trapezoid design is 78.69° (seven-cell-base inlet design). The optimal trapezoid design delivers 0.9 °C lower Max T and 1.17 °C lower ΔT than the rectangular one at 60 L/s flow rate. As a trapezoid layout battery pack design guideline, the optimal length ratio of the outlet to the inlet is suggested to be around 0.7.
- The multi-functional single-layer AHS can be used for both enhancing the battery pack strength and increasing the heat transfer coefficient. The Max T and ΔT values of the optimal trapezoid design with AHS are 4.6 K and 3.78 K lower than the design without AHS at 40 L/s flow rate.
- The novel trapezoid design could be implemented in commercial EV air-cooling BTMS applications by using thin-wall partitions. Theoretically, the modified trapezoid air-cooling BTMS could reduce the Max T and ΔT by 10.4% and 91.9% in addition to a space-saving of about 5.26%.

When there are many battery cells in the real EV application, it is necessary to rearrange the battery cells in a module base to ensure the required cooling performance as proposed in the Discussion section. The feasibility of the proposed modular design needs to be further explored. Nonetheless, the trapezoid pack is promising to improve the cooling performance of the battery pack and can be used as an optimized basic module of a commercial battery pack through simulation studies. The full-scale numerical simulations on the trapezoid battery pack module and experimental investigation are recommended to be conducted in the future works. We are setting up the experimental facilities for this study.

Author Contributions: Conceptualization, G.Z., X.W. and M.N.; methodology, G.Z., X.W., M.N. and H.Z.; supervision, X.W., M.N. and H.Z.; software, G.Z.; validation, G.Z.; formal analysis, G.Z.; investigation, G.Z., X.W., M.N. and C.L.; resources, X.W.; data curation, G.Z.; writing—original draft preparation, G.Z.; writing—review and editing, X.W., M.N., H.Z. and C.L.; project administration, X.W.; funding acquisition, X.W. and M.N. All authors have read and agreed to the published version of the manuscript.

Funding: This research was funded by the Australian Research Council, grant number LP170100879.

Institutional Review Board Statement: Not applicable.

Informed Consent Statement: Not applicable.

Conflicts of Interest: The authors declare no conflict of interest.

Nomenclature

a_n, b_n, . . . , f_n (n = 0, 1, . . . , 5)	constant coefficients
A	battery surface area (m^2)
C	capacitance (F)
C_p	specific heat capacity ($J \cdot kg^{-1} \cdot K^{-1}$)
I	battery current (A)
$\vec{J}$	diffusion flux
j	volumetric transfer current density ($A \cdot m^{-2}$)
k	thermal conductivity ($W \cdot m^{-1} \cdot K^{-1}$)
P, p	pressure (Pa)
Q	battery capacity (Ah)
q	heat generation rate ($W \cdot m^{-3}$)
R	resistance (Ω)
T	temperature (K)
V	battery voltage (V)
$\vec{v}$	air flow velocity vector ($m \cdot s^{-1}$)
Greek symbols	
ρ	mass density ($kg \cdot m^{-3}$)
σ	electrical conductivity ($Siemens \cdot m^{-1}$)
$\bar{\bar{\tau}}$	stress tensor
ϕ	electric potential (V)
φ	electrode phase potential (V)
∇	Del operator used as the partial derivative of a quantity with respect to all directions in the chosen coordinate system (m^{-1})
Subscripts	
a or +	anode
b	battery
c or -	cathode
i, *n* (=1, . . . , N)	arbitrary number
OC	open-circuit

Abbreviations

AHS	aluminum heat spreader
BTMS	battery thermal management system
ECM	electric circuit model
EV	electric vehicle
FSP	field synergy principle
HEV	hybrid electric vehicle
Li-ion	Lithium-ion
Max	maximum
Min	minimum
MSMD	multi-scale multi-domain
OEM	original equipment manufacturer
SoC	state of charge

References

1. Zhang, B. The Effect of Aerosols to Climate Change and Society. *J. Geosci. Environ. Prot.* **2020**, *8*, 55. [CrossRef]
2. Hu, X.; Chen, N.; Wu, N.; Yin, B. The Potential Impacts of Electric Vehicles on Urban Air Quality in Shanghai City. *Sustainability* **2021**, *13*, 496. [CrossRef]
3. Zhao, G.; Wang, X.; Negnevitsky, M. A Study of Variable Cell Spacings to the Heat Transfer Efficiency of Air-Cooling Battery Thermal Management System. *Appl. Sci.* **2021**, *11*, 11155. [CrossRef]
4. Zhao, G.; Wang, X.; Negnevitsky, M. Connecting battery technologies for electric vehicles from battery materials to management. *iScience* **2022**, *25*, 103744. [CrossRef] [PubMed]
5. Zhao, L.; Wang, J.; Li, Y.; Liu, Q.; Li, W. Experimental Investigation of a Lithium Battery Cooling System. *Sustainability* **2019**, *11*, 5020. [CrossRef]
6. Asef, P.; Milan, M.; Lapthorn, A.; Padmanaban, S. Future Trends and Aging Analysis of Battery Energy Storage Systems for Electric Vehicles. *Sustainability* **2021**, *13*, 13779. [CrossRef]
7. Singh, L.K.; Gupta, A.K. Hybrid cooling-based lithium-ion battery thermal management for electric vehicles. *Environ. Dev. Sustain.* **2022**, *24*, 1–22. [CrossRef]
8. Lai, Y.; Wu, W.; Chen, K.; Wang, S.; Xin, C. A compact and lightweight liquid-cooled thermal management solution for cylindrical lithium-ion power battery pack. *Int. J. Heat Mass Transf.* **2019**, *144*, 118581. [CrossRef]
9. Tete, P.R.; Gupta, M.M.; Joshi, S.S. Developments in battery thermal management systems for electric vehicles: A technical review. *J. Energy Storage* **2021**, *35*, 102255. [CrossRef]
10. Tete, P.R.; Gupta, M.M.; Joshi, S.S. Numerical investigation on thermal characteristics of a liquid-cooled lithium-ion battery pack with cylindrical cell casings and a square duct. *J. Energy Storage* **2022**, *48*, 104041. [CrossRef]
11. Murali, G.; Sravya, G.; Jaya, J.; Vamsi, V.N. A review on hybrid thermal management of battery packs and it's cooling performance by enhanced PCM. *Renew. Sustain. Energy Rev.* **2021**, *150*, 111513. [CrossRef]
12. Ikezoe, M.; Hirata, N.; Amemiya, C.; Miyamoto, T.; Watanabe, Y.; Hirai, T.; Sasaki, T. *Development of High Capacity Lithium-Ion Battery for NISSAN LEAF*; SAE Technical Paper; SAE International: Warrendale, PA, USA, 2012; Volume 1, p. 0664. ISSN 0148-7191.
13. Nazari, A.; Farhad, S. Heat generation in lithium-ion batteries with different nominal capacities and chemistries. *Appl. Therm. Eng.* **2017**, *125*, 1501–1517. [CrossRef]
14. Özsin, G.; Dermenci, K.B.; Turan, S. Thermokinetic and thermodynamics of Pechini derived Li 7 − 3x Al x La 3 Zr 2 O 12 (X = 0.0–0.2) xerogel decomposition under oxidative conditions. *J. Therm. Anal. Calorim.* **2021**, *146*, 1405–1420. [CrossRef]
15. Zhao, G.; Wang, X.; Negnevitsky, M.; Zhang, H. A review of air-cooling battery thermal management systems for electric and hybrid electric vehicles. *J. Power Sources* **2021**, *501*, 230001. [CrossRef]
16. Wang, Y.-W.; Jiang, J.-M.; Chung, Y.-H.; Chen, W.-C.; Shu, C.-M. Forced-air cooling system for large-scale lithium-ion battery modules during charge and discharge processes. *J. Therm. Anal. Calorim.* **2019**, *135*, 2891–2901. [CrossRef]
17. Guo, Z.; Liu, X.; Tao, W.; Shah, R. Effectiveness–thermal resistance method for heat exchanger design and analysis. *Int. J. Heat Mass Transf.* **2010**, *53*, 2877–2884. [CrossRef]
18. Adam, A.Y.; Oumer, A.N.; Najafi, G.; Ishak, M.; Firdaus, M.; Aklilu, T.B. State of the art on flow and heat transfer performance of compact fin-and-tube heat exchangers. *J. Therm. Anal. Calorim.* **2020**, *139*, 2739–2768. [CrossRef]
19. Duan, X.-Y.; Li, F.-B.; Ding, B.; Gong, L.; Xu, M.-H. Heat transfer characteristics and field synergy analysis of gas–liquid two-phase flow in micro-channels. *J. Therm. Anal. Calorim.* **2020**, *141*, 401–412. [CrossRef]
20. Tao, W.-Q.; Guo, Z.-Y.; Wang, B.-X. Field synergy principle for enhancing convective heat transfer—-its extension and numerical verifications. *Int. J. Heat Mass Transf.* **2002**, *45*, 3849–3856. [CrossRef]
21. Mahamud, R.; Park, C. Reciprocating air flow for Li-ion battery thermal management to improve temperature uniformity. *J. Power Sources* **2011**, *196*, 5685–5696. [CrossRef]
22. Na, X.; Kang, H.; Wang, T.; Wang, Y. Reverse layered air flow for Li-ion battery thermal management. *Appl. Therm. Eng.* **2018**, *143*, 257–262. [CrossRef]

23. Chen, K.; Song, M.; Wei, W.; Wang, S. Structure optimization of parallel air-cooled battery thermal management system with U-type flow for cooling efficiency improvement. *Energy* **2018**, *145*, 603–613. [CrossRef]
24. Liu, Y.; Zhang, J. Self-adapting J-type air-based battery thermal management system via model predictive control. *Appl. Energy* **2020**, *263*, 114640. [CrossRef]
25. Zhao, J.; Rao, Z.; Huo, Y.; Liu, X.; Li, Y. Thermal management of cylindrical power battery module for extending the life of new energy electric vehicles. *Appl. Therm. Eng.* **2015**, *85*, 33–43. [CrossRef]
26. Hong, S.; Zhang, X.; Chen, K.; Wang, S. Design of flow configuration for parallel air-cooled battery thermal management system with secondary vent. *Int. J. Heat Mass Transf.* **2018**, *116*, 1204–1212. [CrossRef]
27. Zhang, J.; Kang, H.; Wu, K.; Li, J.; Wang, Y. The impact of enclosure and boundary conditions with a wedge-shaped path and air cooling for battery thermal management in electric vehicles. *Int. J. Energy Res.* **2018**, *42*, 4054–4069. [CrossRef]
28. Tao, W.; He, Y.; Wang, Q.; Qu, Z.; Song, F. A unified analysis on enhancing single phase convective heat transfer with field synergy principle. *Int. J. Heat Mass Transf.* **2002**, *45*, 4871–4879. [CrossRef]
29. Li, X.; He, F.; Ma, L. Thermal management of cylindrical batteries investigated using wind tunnel testing and computational fluid dynamics simulation. *J. Power Sources* **2013**, *238*, 395–402. [CrossRef]
30. Wang, T.; Tseng, K.; Zhao, J.; Wei, Z. Thermal investigation of lithium-ion battery module with different cell arrangement structures and forced air-cooling strategies. *Appl. Energy* **2014**, *134*, 229–238. [CrossRef]
31. Yang, N.; Zhang, X.; Li, G.; Hua, D. Assessment of the forced air-cooling performance for cylindrical lithium-ion battery packs: A comparative analysis between aligned and staggered cell arrangements. *Appl. Therm. Eng.* **2015**, *80*, 55–65. [CrossRef]
32. Chen, K.; Wang, S.; Song, M.; Chen, L. Configuration optimization of battery pack in parallel air-cooled battery thermal management system using an optimization strategy. *Appl. Therm. Eng.* **2017**, *123*, 177–186. [CrossRef]
33. Chen, K.; Chen, Y.; She, Y.; Song, M.; Wang, S.; Chen, L. Construction of effective symmetrical air-cooled system for battery thermal management. *Appl. Therm. Eng.* **2020**, *166*, 114679. [CrossRef]
34. Chen, K.; Song, M.; Wei, W.; Wang, S. Design of the structure of battery pack in parallel air-cooled battery thermal management system for cooling efficiency improvement. *Int. J. Heat Mass Transf.* **2019**, *132*, 309–321. [CrossRef]
35. Xu, Y.; Zhang, H.; Xu, X.; Wang, X. Numerical analysis and surrogate model optimization of air-cooled battery modules using double-layer heat spreading plates. *Int. J. Heat Mass Transf.* **2021**, *176*, 121380. [CrossRef]
36. Saw, L.H.; Ye, Y.; Yew, M.C.; Chong, W.T.; Yew, M.K.; Ng, T.C. Computational fluid dynamics simulation on open cell aluminium foams for Li-ion battery cooling system. *Appl. Energy* **2017**, *204*, 1489–1499. [CrossRef]
37. Wang, Y.; Yu, Y.; Jing, Z.; Wang, C.; Zhou, G.; Zhao, W. Thermal performance of lithium-ion batteries applying forced air cooling with an improved aluminium foam heat sink design. *Int. J. Heat Mass Transf.* **2021**, *167*, 120827. [CrossRef]
38. Fan, Y.; Bao, Y.; Ling, C.; Chu, Y.; Tan, X.; Yang, S. Experimental study on the thermal management performance of air cooling for high energy density cylindrical lithium-ion batteries. *Appl. Therm. Eng.* **2019**, *155*, 96–109. [CrossRef]
39. Wang, H.; He, F.; Ma, L. Experimental and modeling study of controller-based thermal management of battery modules under dynamic loads. *Int. J. Heat Mass Transf.* **2016**, *103*, 154–164. [CrossRef]
40. Huo, Y.; Rao, Z. The numerical investigation of nanofluid based cylinder battery thermal management using lattice Boltzmann method. *Int. J. Heat Mass Transf.* **2015**, *91*, 374–384. [CrossRef]
41. Zhang, Y.; Song, X.; Ma, C.; Hao, D.; Chen, Y. Effects of the structure arrangement and spacing on the thermal characteristics of Li-ion battery pack at various discharge rates. *Appl. Therm. Eng.* **2020**, *165*, 114610. [CrossRef]
42. Pesaran, A.A. Battery thermal models for hybrid vehicle simulations. *J. Power Sources* **2002**, *110*, 377–382. [CrossRef]
43. Zhao, C.; Cao, W.; Dong, T.; Jiang, F. Thermal behavior study of discharging/charging cylindrical lithium-ion battery module cooled by channeled liquid flow. *Int. J. Heat Mass Transf.* **2018**, *120*, 751–762. [CrossRef]
44. Zhao, C.; Sousa, A.; Jiang, F. Minimization of thermal non-uniformity in lithium-ion battery pack cooled by channeled liquid flow. *Int. J. Heat Mass Transf.* **2019**, *129*, 660–670. [CrossRef]
45. Patil, M.S.; Seo, J.-H.; Panchal, S.; Jee, S.-W.; Lee, M.-Y. Investigation on thermal performance of water-cooled Li-ion pouch cell and pack at high discharge rate with U-turn type microchannel cold plate. *Int. J. Heat Mass Transf.* **2020**, *155*, 119728. [CrossRef]
46. Ye, Y.; Shi, Y.; Saw, L.H.; Tay, A.A. Performance assessment and optimization of a heat pipe thermal management system for fast charging lithium ion battery packs. *Int. J. Heat Mass Transf.* **2016**, *92*, 893–903. [CrossRef]
47. Monika, K.; Chakraborty, C.; Roy, S.; Dinda, S.; Singh, S.A.; Datta, S.P. Parametric investigation to optimize the thermal management of pouch type lithium-ion batteries with mini-channel cold plates. *Int. J. Heat Mass Transf.* **2021**, *164*, 120568. [CrossRef]
48. Saw, L.H.; Poon, H.M.; Thiam, H.S.; Cai, Z.; Chong, W.T.; Pambudi, N.A.; King, Y.J. Novel thermal management system using mist cooling for lithium-ion battery packs. *Appl. Energy* **2018**, *223*, 146–158. [CrossRef]
49. Lindgren, J.; Lund, P.D. Effect of extreme temperatures on battery charging and performance of electric vehicles. *J. Power Sources* **2016**, *328*, 37–45. [CrossRef]
50. Waldmann, T.; Wilka, M.; Kasper, M.; Fleischhammer, M.; Wohlfahrt-Mehrens, M. Temperature dependent ageing mechanisms in Lithium-ion batteries—A Post-Mortem study. *J. Power Sources* **2014**, *262*, 129–135. [CrossRef]
51. Leng, F.; Tan, C.M.; Pecht, M. Effect of Temperature on the Aging rate of Li Ion Battery Operating above Room Temperature. *Sci. Rep.* **2015**, *5*, 12967. [CrossRef]

52. Sheng, L.; Su, L.; Zhang, H.; Li, K.; Fang, Y.; Ye, W.; Fang, Y. Numerical investigation on a lithium ion battery thermal management utilizing a serpentine-channel liquid cooling plate exchanger. *Int. J. Heat Mass Transf.* **2019**, *141*, 658–668. [CrossRef]
53. Zou, D.; Ma, X.; Liu, X.; Zheng, P.; Hu, Y. Thermal performance enhancement of composite phase change materials (PCM) using graphene and carbon nanotubes as additives for the potential application in lithium-ion power battery. *Int. J. Heat Mass Transf.* **2018**, *120*, 33–41. [CrossRef]
54. Yan, J.; Wang, Q.; Li, K.; Sun, J. Numerical study on the thermal performance of a composite board in battery thermal management system. *Appl. Therm. Eng.* **2016**, *106*, 131–140. [CrossRef]
55. Shang, Z.; Qi, H.; Liu, X.; Ouyang, C.; Wang, Y. Structural optimization of lithium-ion battery for improving thermal performance based on a liquid cooling system. *Int. J. Heat Mass Transf.* **2019**, *130*, 33–41. [CrossRef]
56. Choudhari, V.; Dhoble, A.; Panchal, S. Numerical analysis of different fin structures in phase change material module for battery thermal management system and its optimization. *Int. J. Heat Mass Transf.* **2020**, *163*, 120434. [CrossRef]
57. Pan, M.; Zhong, Y. Experimental and numerical investigation of a thermal management system for a Li-ion battery pack using cutting copper fiber sintered skeleton/paraffin composite phase change materials. *Int. J. Heat Mass Transf.* **2018**, *126*, 531–543. [CrossRef]
58. Tiedemann, W.; Newman, J. Mathematical modeling of the lead-acid cell. In *Proceedings of the Symposium on Battery Design and Optimization*; The Electrochemical Society: Princeton, NJ, USA, 1979; Volume 79.
59. Lee, K.-J.; Smith, K.; Pesaran, A.; Kim, G.-H. Three dimensional thermal-, electrical-, and electrochemical-coupled model for cylindrical wound large format lithium-ion batteries. *J. Power Sources* **2013**, *241*, 20–32. [CrossRef]
60. Chen, M.; Rincon-Mora, G.A. Accurate Electrical Battery Model Capable of Predicting Runtime and I–V Performance. *IEEE Trans. Energy Convers.* **2006**, *21*, 504–511. [CrossRef]
61. Pinto, A.M.; Oliveira, V.S.; Falcão, D.S.C. *Direct Alcohol Fuel Cells for Portable Applications: Fundamentals, Engineering and Advances*; Academic Press: Cambridge, MA, USA, 2018.
62. Barbir, F. *PEM Fuel Cells: Theory and Practice*; Academic Press: Cambridge, MA, USA, 2012.
63. Yang, Y.; Chen, L.; Yang, L.; Du, X. Numerical study of combined air and phase change cooling for lithium-ion battery during dynamic cycles. *Int. J. Therm. Sci.* **2021**, *165*, 106968. [CrossRef]